DTU Library

AI-Based Design with Data Trimming for Hybrid Phase Shift Modulation for Minimum-Current-Stress Dual Active Bridge Converter

Lin, Fanfan; Zhang, Xin ; Li, Xinze ; Sun, Changjiang ; Zsurzsan, Tiberiu Gabriel; Cai, Wenjian ; Wang, Chang

AI-Based Design with Data Trimming for Hybrid Phase Shift Modulation for Minimum-Current-Stress Dual Active Bridge Converter

Fanfan Lin, *Student Member*, *IEEE*, Xin Zhang, *Senior Member*, *IEEE*, Xinze Li, *Student Member*, *IEEE*, Changjiang Sun, *Member*, *IEEE*, Gabriel Zsurzsan, *Member*, *IEEE*, Wenjian Cai, *Member*, *IEEE,* Chang Wang, *Student Member*, *IEEE*.

Abstract—Dual active bridge (DAB) topology has been recognized as the key circuit for the next generation of high-frequency-link power conversion systems. In order to realize desired operating performance, DAB modulation strategies need to be selected carefully. Different modulation strategies have been considered and combined into a hybrid one, which is able to fully optimize performance. However, to develop a hybrid modulation strategy, the conventional methods including harmonic model and piecewise model have difficulty in balancing modeling accuracy and manpower burden. Although recent data-driven modulation approaches can automate the design process, the accuracy of data-driven models decreases nontrivially with the existence of outliers and without sufficient data. Hence, to alleviate human-dependence and improve modeling accuracy, this paper proposes an AI-based design with data trimming (AI-DT) for hybrid phase shift modulation. Two two-degree-of-freedom modulation strategies are considered for the sake of optimal current stress performance. AI-DT firstly adopts the one-class support vector machine (SVM) to exclude outliers. Second, the state-of-the-art extreme gradient boosting (XGBoost), which is insensitive to training data size, is adopted to build data-driven current stress models for the DAB converter. After that, differential evolution (DE) algorithm helps to choose modulation strategy and optimize modulation parameters for optimal current stress. Generally, the proposed AI-DT is developed in an automated fashion, which largely relieves manual computational complexity while exhibiting satisfactory modulation accuracy. The effectiveness of the proposed AI-DT approach has been experimentally verified with a 1kW hardware prototype, realizing optimal current stress under full operating conditions with more than 96.5% as peak efficiency.

Index Terms—dual active bridge, phase shift modulation, hybrid modulation, current stress, artificial intelligence, outlier detection, XGBoost, differential evolution algorithm.

Xinze Li, Changjiang Sun, and Wenjian Cai are with the School of Electrical and Electronic Engineering, Nanyang Technological University, Singapore 639798, Singapore. (e-mail: xinze001@e.ntu.edu.sg; changjiang.sun@ntu.edu.sg; ewjcai@ntu.edu.sg).

Xin Zhang is with the College of Electrical Engineering, Zhejiang University, Hangzhou 310027, China, and with Hangzhou Global Scientific and Technological Innovation Center, Zhejiang University, Hangzhou 310058, China. (e-mail: zhangxin_ieee@163.com).

Fanfan Lin is with ERI@N, Interdisciplinary Graduate Program, Nanyang Technological University, Singapore 639798, Singapore. (e-mail: fanfan001@e.ntu.edu.sg).

Gabriel Zsurzsan and Chang Wang are with the Department of Electrical Engineering, Technical University of Denmark, Kgs. Lyngby 2800, Denmark. (e-mail: tgzsur@elektro.dtu.dk; chawa@elektro.dtu.dk).

I. INTRODUCTION

Firstly proposed in the early 1990s [1], dual active bridge (DAB) topology has been recognized as the key circuit for the next generation high-frequency-link power conversion systems [2], [3]. Without line-frequency transformers, it features light weight and compact size. Moreover, other advantages of the DAB converter include bidirectional power transfer capability, high power density and ease to realize zero voltage switching (ZVS) [4]. Nowadays, DAB converters can be found in various applications like battery energy storage systems [5], back-to-back systems [6], solid state transformers [7], [8], electric vehicles [9], etc.

Among the emerging research works regarding DAB converters, modulation strategy is an important topic as it can achieve flexible power control and enhance operating performance. Single phase shift modulation (SPS) [10] is a classical modulation strategy for DAB converters which adjusts the outer phase shift between the primary full bridge and the secondary full bridge. SPS modulation is easy to implement, however, it fails to achieve a wide ZVS range and satisfactory efficiency performance. To relieve these pains, one more degree of freedom, which is the inner phase shift of the full bridge, is added to SPS to realize dual phase shift (DPS) [11] and extended phase shift (EPS) modulation [12], [13]. If two inner phase shifts of two full bridges are set as independently adjustable parameters, it becomes triple phase shift (TPS) modulation [14]. TPS has three degrees of freedom and can be regarded as the generalized version of SPS, DPS and EPS.

To realize the best performance of DAB converters in the full operating range, some researchers work on hybrid modulation (HM) strategies. Shen *et al.* applied EPS and TPS to achieve practical ZVS operation of all switches over the full operating range while minimizing the conduction losses [15]. Amit *et al.* explored the combination of different modes of TPS to achieve the highest efficiency over a wide operating range [16]. A more complicated hybrid duty modulation was introduced by Di *et al.*, which added two more degrees of freedom based on TPS to minimize rms current and extend the soft-switching range [17].

Nevertheless, the conventional design of a HM suffers from massive human-dependence, resulting in time-consuming model building and optimization processes and inaccurate models. For example, to optimize the current stress to protect power devices and achieve high efficiency, the conventional

design method will first build models with harmonic model or piecewise model. On one hand, the harmonic model has low accuracy because only the fundamental component is considered. On the other hand, the piecewise model is complicated in that it requires manual derivation for every different operating mode in one modulation strategy. If a HM is considered, expression derivation needs to be done manually for every single modulation strategy. After models are built, the complex current stress expressions, consisting of higher order nonlinear terms, will be optimized with mathematical approximations or numerical algorithms, both of which can decrease the modeling accuracy. Thus, the complexity of conventional design approaches will be too high when the optimization of current stress is considered in a HM strategy because of the heavy computation both in model building and optimization. Moreover, the issue of poor modeling accuracy may occur resulting from mathematical approximations or inaccurate algorithms. How to ameliorate the heavy computation due to massive human-dependence and achieve high modeling accuracy simultaneously is the main focus of this paper.

Recently, stepping into the era of artificial intelligence, more and more researchers in power electronics are considering adopting artificial intelligence (AI) tools to accelerate and automate such complex model building and optimization processes. The prevailing computer-aided approaches take advantage of AI algorithms to optimize power converter designs. For instance, for the circuit parameter design of a CLLC-type DAB converter, a latest particle swarm optimization (PSO) variant is adopted to optimize cascaded gain margin and efficiency while considering parameter fluctuations [18]. In [19], mathematical hybrid automation describes the constrained state-space equations of various modes to optimize the phase shift modulation of DAB converters for optimal current stress performance. Besides, reinforcement learning techniques have been applied for the optimization of modulation strategies for various objectives, such as optimal reactive power [20], minimum current stress [21], etc.

These computer-aided design approaches are limited to automate optimization process, but the model building process which occupies the majority of development time remains human dependent. To automate such time-consuming model building process, data-driven approaches are gaining popularity. For example, Qun *et al.* made use of deep belief network, a generative graphical deep learning model, to realize fault diagnosis for a closed-loop single-ended primary inductance converter [22]. To stabilize voltage of dc-dc converters in dc microgrids, Mojtaba *et al.* adopted deep reinforcement learning technique [23]. Neural network (NN) has also been used in the realization of TPS modulation for DAB converters [24]. [25] adopted feedforward NN for the accurate modeling of efficiency of buck converters. Li *et al.* utilized NN to replace manual performance derivation and optimization [26]. [27] applied AI algorithms for efficiency-oriented optimization for DAB converters under TPS modulation.

However, most of the AI techniques used to automate the model building and optimization processes are inappropriate due to some unneglectable disadvantages. Foremost, the common existence of outliers is not considered, which can seriously undermine the learning accuracy as discussed in [28]. Due to the presence of outliers, the modeling accuracy of latest NN-based design approaches like [26] and [27] suffers. Consequently, how to exclude the abnormal data to improve the modeling accuracy is also a focus of this paper.

Except for failing to consider data abnormality, most AI algorithms are sensitive to training data size, resulting in either underfitting or overfitting. If a shallow NN or a simple decision tree is applied, it is prone to underfitting because of insufficient learning capacity. While a deep NN may have an overfitting problem for learning the training data too well and require large set of data and heavy computation [29]. Hence, an AI technique that is flexible with data size and has good accuracy is expected in the application for power electronics.

On the basis of the aforementioned analysis, outlier detection and data trimming are leveraged to improve modeling accuracy. In electrical engineering, outlier detection techniques are mostly used for condition monitoring, such as the machinery condition monitoring [30], battery reliability testing [31], metering equipment monitoring [32], etc. In this paper, the one-class support vector machine (SVM) is specially selected by virtue of its high performance for detecting outliers and low algorithm complexity. Moreover, a promising AI algorithm, the extreme gradient boosting (XGBoost) proposed by Chen and Guestrin in 2016 [33], is adopted since it can attain satisfactory modeling accuracy with significantly less training data than deep learning approaches, and it is light in computation and free from overfitting.

In this research work, we propose an AI-based design with data trimming (AI-DT) for a hybrid phase shift modulation for DAB converters with optimal current stress. In this HM strategy, EPS and DPS are considered for different operating conditions, both of which have two degrees of freedom. This choice can balance the optimal operating performance and the ease of implementation. The proposed AI-DT approach consists of two phases. In Phase One, training data is generated with simulation software, and one-class SVM algorithm is utilized to trim abnormal data points, alleviating the severity of outliers. After the data trimming, XGBoost, as one of the state-of-the-art AI techniques, is applied to build data-driven current stress models for EPS and DPS modulation strategies. In Phase Two, differential evolution (DE) algorithm is adopted to find optimal hybrid modulation parameters to achieve minimum current stress. In a nutshell, AI-DT has the following merits:

- First, AI-DT is executed automatically, pointing out the potential way forward for applying AI techniques to automate and accelerate the development of modulation strategies in power converters.
- Second, the current stress performance of the HM will be optimal compared to any single two-degree-of-freedom modulation strategy.
- Third, the influence of abnormal data is studied, and the data-driven modeling accuracy is improved since the adopted one-class SVM excludes harmful outliers.
- Fourth, the carefully selected XGBoost model is more appropriate than other ML techniques, attaining good

accuracy with less data required.

This paper is organized as follows. Detailed explanations about EPS and DPS modulation strategies, and the conventional methods and challenges to model current stress are elaborated in Section II and III, respectively. Section IV, and V present Phase One, and Two of the proposed AI-DT, respectively. In Section VI, one detailed case study is illustrated according to the provided specifications. To validate the effectiveness of AI-DT, experimental results are analyzed in Section VII. Finally, the conclusion of this paper is summarized in Section VIII.

II. OPERATING PRINCIPLE OF EPS AND DPS MODULATIONS

A. Topology of DAB Converter

The topology of DAB converter is described with Fig. 1. A high frequency transformer connects two full bridges together. It realizes galvanic isolation and transfers power. The turn ratio of the transformer is n. v_{AB} and v_{CD} are defined as the ac voltages of primary and secondary full bridges, respectively. i_L is the current through the leakage inductor of the transformer (L_k).
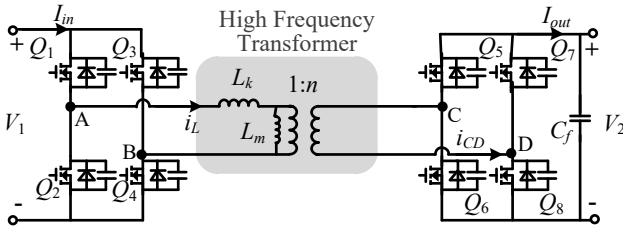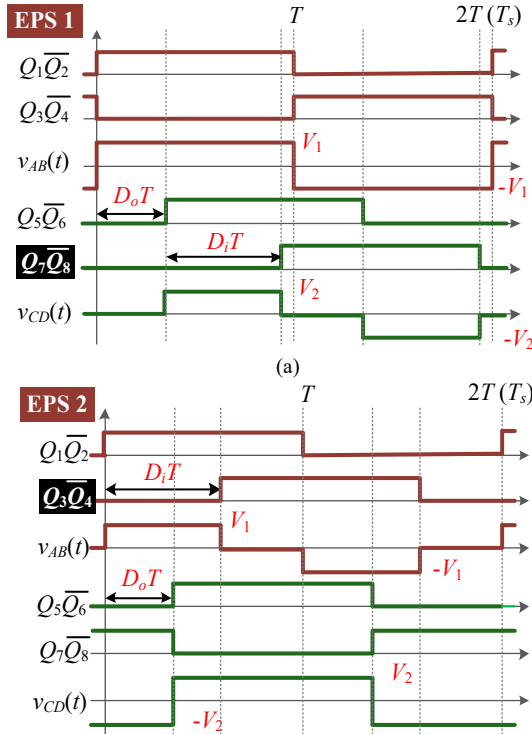

Fig. 1. Topology of the DAB converter.

Fig. 2. EPS modulation scheme: (a) EPS1; (b) EPS2.

B. Operating Principles of EPS Modulation

In EPS modulation, there are two degrees of freedom, outer phase shift D_o and inner phase shift D_i. If D_i is applied to the secondary full bridge, we name it EPS1 and if it is applied to the primary full bridge, we refer to it as EPS2.

Fig. 2 illustrates the gate drive sequences of switches and definition of two phase shift parameters in EPS. The upper and lower switches in each switching leg are driven with 50% duty cycle complementarily when dead time is neglected. T_s is the switching period and T is half of T_s [12]. In both kinds of EPS modulation, D_o shares the same definition, which is the phase shift between the primary full bridge and the secondary full bridge (Q_1 and Q_5). The adjustable range of D_o is [-1, 1]. As shown in two black text blocks in Fig. 2, the full bridge where D_i is applied is the difference between EPS1 and EPS2. In EPS1, the secondary full bridge has an inner phase shift D_i and Q_7 will have a D_iT time delay compared to Q_5. In this case, v_{CD} is a three-level voltage waveform. Conversely, in EPS2, the primary full bridge has an inner phase shift D_i and Q_3 will have a D_iT time delay compared to Q_1. And in this situation, v_{AB} is a three-level voltage wave. Thanks to the zero voltage plateaus of the three-level wave, backflow power is zero which decreases the circulating power. Both in EPS1 and EPS2, the adjustable range of D_i is [0, 1]. To achieve the decreased circulating power, when the voltage conversion state is boost or buck mode, EPS1 or EPS2 will be selected accordingly [34], [35]. Compared to traditional SPS modulation, EPS modulation shows better efficiency and current stress performance as well as wider ZVS operating range [36], [37].

C. Operating Principles of DPS Modulation

DPS modulation also has two degrees of freedom, outer phase shift D_o and inner phase shift D_i. In contrast to EPS modulation, its D_i applies to both of the full bridges.

Fig. 3 describes the gate drive sequences of switches and definition of two phase shift parameters in DPS. The upper and lower switches in each switching leg are still driven with 50% duty cycle complementarily when dead time is neglected. D_o shares the same definition and adaptable range as that in EPS. The primary full bridge and secondary full bridge both have an inner phase shift D_i, which means Q_3 and Q_7 will have a D_iT time delay compared to Q_1 and Q_5, respectively [11]. As shown in Fig. 3, v_{AB} and v_{CD} of both bridges are three-level voltage waveforms. The adjustable range of D_i is [0, 1]. Compared to SPS modulation, DPS is also able to decrease current stress, improve efficiency and expand ZVS operating range [38], [39].
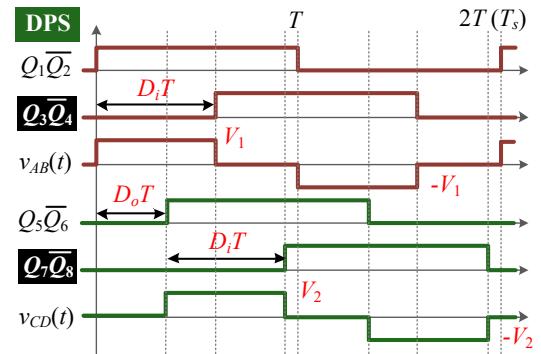

Fig. 3. DPS modulation scheme.

In EPS and DPS modulations, the transferred maximum power can both be calculated with (1) where f_s is the switching frequency. And accordingly, the design range of L_k can be calculated with (2).

$$P_{max} = \frac{nV_1V_2}{8f_sL} \tag{1}$$

$$L_k \leq \frac{nV_1V_2}{8f_sP_{max}} \tag{2}$$

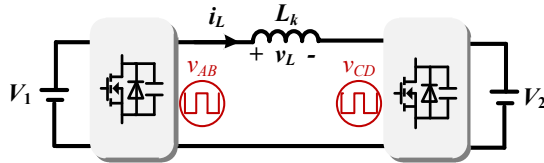## III. CONVENTIONAL MODELING METHODS OF CURRENT STRESS

Fig. 4. Equivalent circuit of a single-inductor non-resonant DAB converter.

Generally, two methods are usually considered to build the steady-state models for the DAB converter: the harmonic model and the piecewise model. In this paper, current stress is evaluated with the peak-to-peak current through L_k (I_{pk}).

A. Harmonic Model

Fig. 4 gives the equivalent circuit of a single-inductor non-resonant DAB converter, from which we can find that v_{AB} and v_{CD} are high-frequency square waves.

In the harmonic model, v_{AB} and v_{CD} are expressed with the Fourier series transformation. A unified model for EPS and DPS modulations is provided by [40]:

$$\begin{cases} v_{AB}(t) = \sum_{n=1,3,5,...} \frac{4V_1}{n\pi}\cos\left(n\frac{\beta_{i1}}{2}\right)\sin\left(n\omega_0 t\right) \\ v_{CD}(t) = \sum_{n=1,3,5,...} \frac{4V_2}{n\pi}\cos\left(n\frac{\beta_{i2}}{2}\right)\sin\left(n\left(\omega_0 t - \beta_o\right)\right) \end{cases}, \tag{3}$$

in which β_o is the outer phase shift angle, and β_{i1} and β_{i2} are the inner phase shift angles for primary and secondary full bridges, respectively. In EPS modulation, only one of β_{i1} and β_{i2} is equal to zero. While in DPS modulation, β_{i1} is equal to β_{i2}. Based on (3), the voltage across L_k (v_L) can be expressed as v_{AB} - v_{CD}. After that, i_L can be obtained by dividing v_L by the impedance of L_k. And then I_{pk} can be calculated accordingly by taking the peak-to-peak value of i_L.
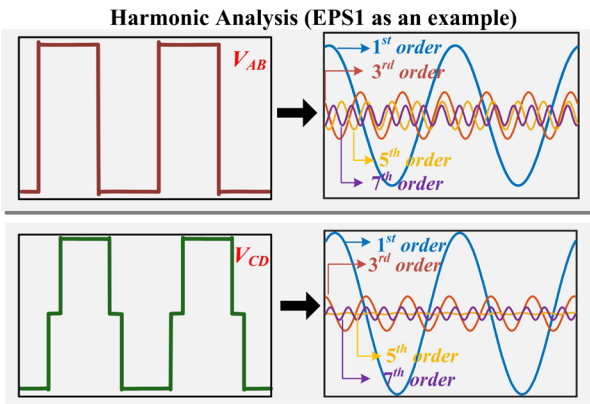

Fig. 5. Descriptions on building harmonic models.

Fig. 5 gives a visual representation of harmonic model analysis, taking v_{AB} and v_{CD} in EPS1 as an example. Because of space limitations, only 1st, 3rd, 5th and 7th harmonics are displayed. But in reality, it has infinite orders of harmonics.

Thus, the pain point of the harmonic model is the trade-off between modeling accuracy and computational load. It is extremely hard to calculate all components of the harmonics, but when only the fundamental component is considered, accuracy is compromised.

B. Piecewise Model

The other frequently used model is the piecewise model. As the name suggests, this method analyzes i_L piece by piece within one switching period through the inductor volt-second balance principle [41], [42]. $i_L(t)$ of every time segment in every operating mode is derived individually. Fig. 6 gives an example of piecewise analysis, which segments i_L in DPS modulation into 8 parts.

This method, even though performs better than the harmonic model with regards to modeling accuracy, the derivation of I_{pk} takes a lot of manual efforts as it requires the analysis of $i_L(t)$ in every time segment for all operating modes and modulation strategies.

Piecewise Analysis (DPS as an example)

Segment	$[t_1, t_2]$	$[t_2, t_3]$	$[t_3, t_4]$	$[t_4, t_5]$	$[t_5, t_6]$	$[t_6, t_7]$	$[t_7, t_8]$	$[t_8, t_9]$
v_{AB}	0	V_1	V_1	0	0	$-V_1$	$-V_1$	0
v_{CD}	0	0	V_2	V_2	0	0	$-V_2$	$-V_2$

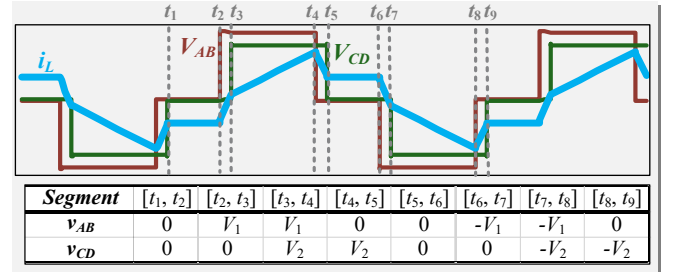Fig. 6. Descriptions on building piecewise models.

C. Challenges of Existing Modeling Methods

Overall, the conventional harmonic and piecewise modeling methods suffer from heavy computation induced by sophisticated derivation process and poor modeling accuracy due to limited harmonics or mathematical approximations, which are summarized in Fig. 7. How to automate the human-dependent modeling process to free manpower burden while keeping high modeling accuracy is the main challenge of this paper.

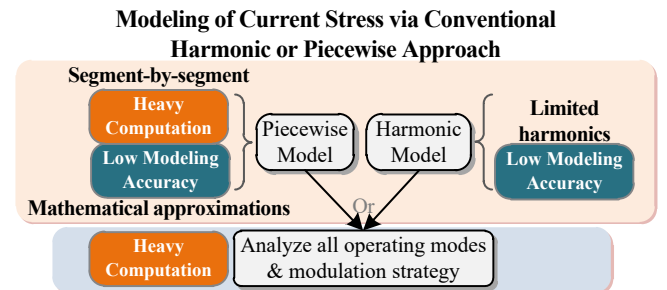**Modeling of Current Stress via Conventional Harmonic or Piecewise Approach**

Fig. 7. Challenges of conventional modeling methods.

Although recent NN-based data-driven approaches [24], [26], [27] can alleviate human-dependence, the lack of considerations of data outliers and the sensitivity to data size will reduce

modeling accuracy. As shown in Fig. 8, data outliers will lead to deviated behaviors, and the accuracy of NN drops with the decrease of training data size. Consequently, this paper aims at mitigating the negative impacts of abnormal data points and ensuring that the data-driven model is robust to data size.
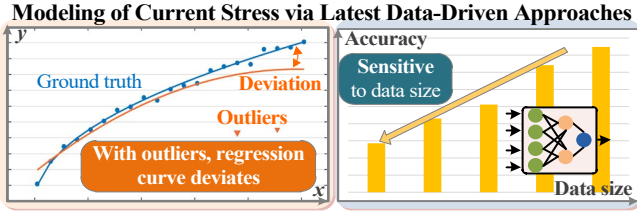

Fig. 8. Challenges of recent data-driven modeling methods.

IV. THE PROPOSED AI-DT PHASE ONE: BUILD DATA-DRIVEN CURRENT STRESS MODELS WITH DATA TRIMMING

This paper proposes a two-stage AI-DT, which is conducted in a fully automated fashion to ameliorate heavy manual derivation. In this section, Phase One of the proposed AI-DT is introduced, which is to build data-driven current stress models with the data trimming technique and the advanced XGBoost algorithm. Detailed steps in Phase One will be explained first, followed by illustrations of the operating principles of the one-class SVM for data trimming and the XGBoost for data-driven modeling.

A. Phase One: Build Data-Driven Current Stress Models

Phase One aims to build data-driven models for current stress of DAB converters under different modulation strategies. With the integration of simulation software, one-class SVM and the specially adopted XGBoost model, the surrogate models of current stress under different operating conditions and modulation strategies are automatically built. The steps of Phase One shown in Fig. 9 is illustrated in detail as the following.
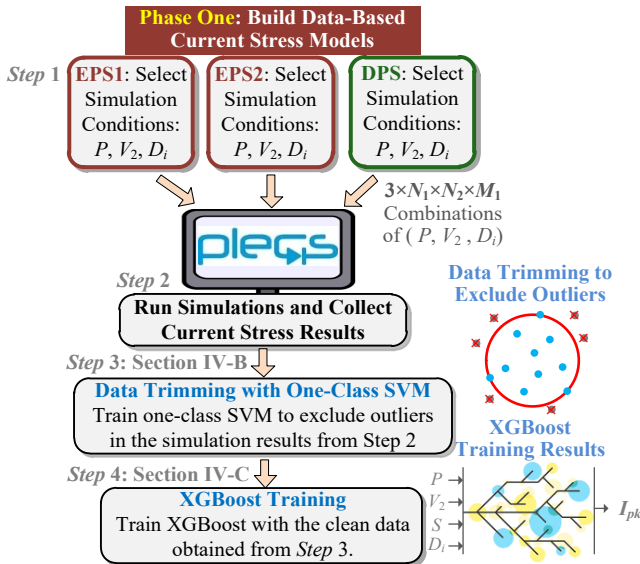

Fig. 9. Flowchart of Phase One of AI-DT.

Before the start of Phase One, the operating conditions must be specified, including input voltage V_1, range of output voltage $[V_{2min}, V_{2max}]$, range of power transferred $[P_{min}, P_{max}]$ and switching frequency.

After these preparations, Phase One will follow the flowchart below, which consists of four steps.

In Step 1, combinations of simulation conditions need to be determined for both EPS1, EPS2 and DPS modulations. These combinations will be used for running simulations in Step 2. Simulation conditions include operating parameters (power transferred P and output voltage V_2), modulation strategy (S), and modulation parameters D_i. P, V_2 and D_i can be uniformly sampled within the range $[P_{min}, P_{max}]$, $[V_{2min}, V_{2max}]$ and $[0, 1]$, respectively. S will be chosen among EPS1, EPS2 and DPS modulation strategies. The number of samples for P, V_2 and D_i is N_1, N_2, M_1 and thus total number of combinations will be $3 \times N_1 \times N_2 \times M_1$.

In Step 2, a simulation model is built in PLECS [43], [44] and it runs for $3 \times N_1 \times N_2 \times M_1$ combinations of operating conditions, which are decided in Step 1. PLECS is chosen because it has high simulation accuracy while maintaining the fast simulation speed attributable to lookup tables. The current stress results (I_{pk}) provided by the simulation are trimmed in Step 3.

In Step 3, a popular outlier detection algorithm, the one-class SVM algorithm, is used to exclude abnormal current stress results. One-class SVM finds a hyper-sphere decision boundary that incorporates normal data and excludes abnormal data. The clean training data after the data trimming is given to Step 4 for data-driven modeling of current stress performance.

In the last step, a data-driven current stress model, XGBoost, is trained. During training, XGBoost will learn the relationships between inputs (P, V_2, S, D_i) and output (I_{pk}). Strategy selector S encodes the considered modulation strategies. By specifying different values of S, the current stress performance of different modulation strategies can be evaluated. After training, it will become a surrogate model for current stress under hybrid modulation strategy, which is able to evaluate current stress performance under any operating condition and modulation strategy within the specified ranges.

B. Application of One-Class SVM in AI-DT for Data Trimming
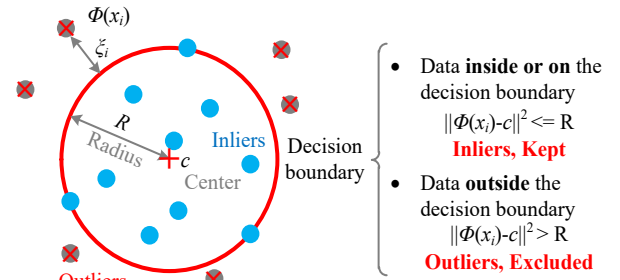

Fig. 10. Principle of the one-class SVM for data trimming.

In AI-DT, to prevent outliers from reducing the data-driven modeling accuracy, the one-class SVM algorithm is specially adopted. The one-class SVM maps the data points to a higher dimensional feature space and finds a hyper-sphere that includes normal data and excludes outliers. As shown in formula (4) and Fig. 10, the radius R of hyper-sphere is minimized, where c is the center, Φ is the feature mapping function, ξ_i is a slack variable to consider soft margin, l is the total number of data,

and υ is a parameter controlling the length of R. The one-class SVM is carefully adjusted to exclude most outliers, benefiting the accuracy of the proposed data-driven modeling approach.

$$\min\left(R^2 + \frac{1}{\upsilon l}\sum_i \xi_i \right)$$
$$s.t. \ \left\| \Phi(x_i) - c \right\|^2 \leq R^2 + \xi_i, \xi_i \geq 0 \tag{4}$$

C. Application of XGBoost in AI-DT for Data-Driven Modeling

XGBoost, which is an ensemble learning algorithm based on decision trees, is used rather than NN for regression purpose because of the following distinctive advantages. First, XGBoost is not data intensive, which means that it can attain high modeling accuracy with less data required compared with NN. Second, XGBoost consists of a series of weak decision trees, so overfitting is greatly relieved. Moreover, the structure of XGBoost can be easily adjusted [33]. With XGBoost, high modeling accuracy and light computation load are achieved simultaneously. The training process of XGBoost is described with Fig. 11.
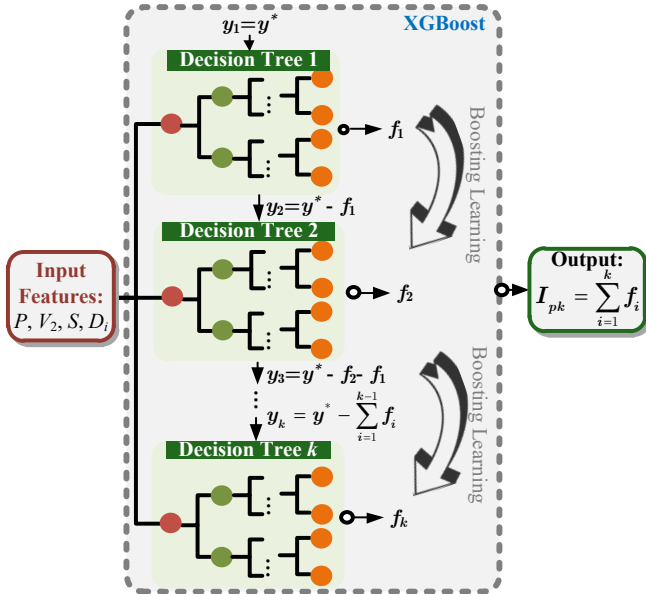

Fig. 11. Schematic diagram of XGBoost

XGBoost contains k decision trees, and each tree aims to learn y_k, which is the residual between the target output value y^* and the cumulative outputs of all previous trees. To take the first decision tree as an example, target output value y^* is compared with the output of Decision Tree 1 (f_1) and the corresponding residual is marked as y_2. With boosting learning strategy, y_2 will be marked as the target output value for Decision Tree 2 and compare with the output f_2 to obtain the residual y_3 for the next tree. This rule applies to other trees. To generate the kth tree, the objective function in (5) is minimized to tune the learnable parameters θ_k of this tree. When obj_k is minimized, the output of the kth tree (f_k) will get closer to y_k. The final output of the XGBoost system can be obtained by summing up the outputs of all decision trees.

In our case, the target output value y^* is equal to the targeted value of I_{pk}^* and final output of this XGBoost system is the predicted value of I_{pk} for the specified input features (P, V_2 and D_i), expressed with (6).

$$\min_{\theta_k}\left(obj_k\right) = \min_{\theta_k}\left(y_k - f_{k,\theta_k}\right)^2 = \min_{\theta_k}\left(y^* - \sum_i^{k-1} f_i - f_{k,\theta_k}\right)^2 \tag{5}$$

$$I_{pk}\left(P,V_2,S,D_i\right) = \sum_{i=1}^{k} f_i\left(P,V_2,S,D_i\right) \tag{6}$$

In summary, with the application of XGBoost in Phase One, a data-driven current stress model can be obtained without any complicated mathematical derivation.

V. THE PROPOSED AI-DT PHASE TWO: OPTIMIZE CURRENT STRESS WITH DIFFERENTIAL EVOLUTION ALGORITHM

This section introduces Phase Two of the proposed AI-DT, which is to find the best modulation strategy and optimize modulation parameters with differential evolution (DE) algorithm [45]. In Phase Two, the DE algorithm interacts with the trained XGBoost surrogate models of current stress from Phase One to automatically optimize modulation parameters.

DE is selected due to its robust and consistent optimization performance and fast computation speed [46]. Compared to genetic algorithm which is suitable for discrete optimization, DE is designed for solving continuous optimization since it is founded on vector arithmetic. Compared to PSO, DE can enhance population diversification to improve optimization performance since candidate solutions are not affected by the global best solution. Moreover, being beneficial from the floating-point arithmetic, DE exhibits fast computation speed.
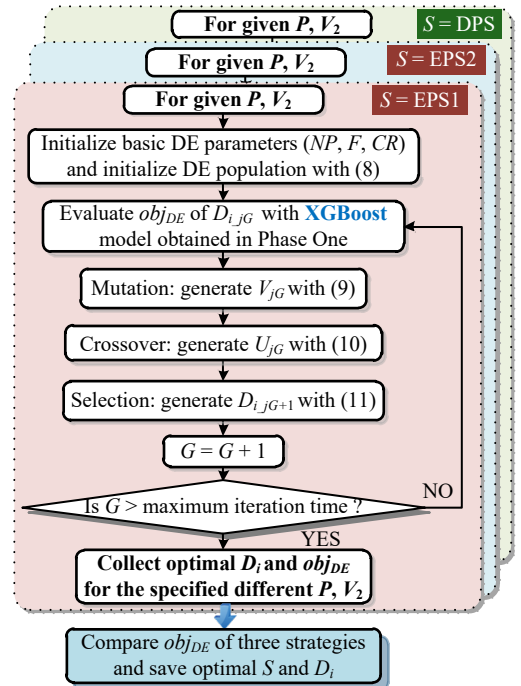

Fig. 12. Flowchart of Phase Two.

DE algorithm is composed of three evolutionary operators, which are mutation, crossover and selection [47], [48]. Mutation is used to add weighted difference to reference individual to create a mutant individual. Crossover generates a new

individual based on the mutant individual and a current individual. And selection is used to evaluate the performance of this new individual and choose between it and the current individual.

In our case, for specified P and V_2, DE will search for the optimal D_i value and optimal current stress performance for EPS1, EPS2 and DPS modulation strategies. The objective for DE is expressed with (7). After that, the optimal current stress performance of these three strategies will be compared and the best strategy is selected. On the basis of the XGBoost model obtained in Phase One, Phase Two will apply DE algorithm with the flowchart in Fig. 12.

Under selected P and V_2, the objective is:

$$\min_{D_i}\left(obj_{DE}\right) = \min_{D_i}\left(I_{pk}(S, D_1, P_{out}, V_2)\right) \tag{7}$$

Subject to:

$$S \in \left[\text{EPS1, EPS2, DPS}\right] \tag{7a}$$

$$0 \le D_i \le 1 \tag{7b}$$

Under one modulation strategy S, firstly, some DE parameters need to be initialized, including population size NP, differential weight F and crossover probability CR. The individual of the population in generation G is written as D_{i_jG} where $j \in [1, 2, \cdots, NP]$. Initialization of the whole population follows (8), in which D_{i_min} is 0 and D_{i_max} is 1. $rand(0, 1)$ is a random variable within the range of (0, 1). After evaluation of obj_{DE} of the population, DE performs mutation operations to generate V_{jG} with formula (9), where D_{i_bestG} is the best individual in generation G with lowest obj_{DE} value. This will be followed by a crossover operation with formula (10). The crossover result U_{jG} will be compared with the current individual D_{i_jG} with regards to obj_{DE} during the selection operation, as described with (11). Finally, termination of this algorithm is based on the iteration times. Among EPS1, EPS2 and DPS, the modulation strategy and corresponding D_i which contribute to lowest obj_{DE} will be saved for the specified P and V_2.

$$D_{i\_j0} = rand(0,1) \times \left(D_{i\_\max} - D_{i\_\min}\right) + D_{i\_\max} \tag{8}$$

$$V_{jG} = D_{i\_bestG} + F \times \left(D_{i\_r1G} - D_{i\_r2G}\right) \text{where } r_1, r_2 \in \left[1, NP\right] \tag{9}$$

$$U_{jG} = \begin{cases} V_{jG}, & \text{if } rand(0,1) \le CR \\ D_{i\_jG}, & \text{otherwise} \end{cases} \tag{10}$$

To conclude this section, for any given P and V_2 condition, the optimal modulation strategy S and optimal modulation parameter D_i can be obtained by following Phase Two.

$$D_{i\_jG+1} = \begin{cases} U_{jG}, & \text{if } obj_{DE}\left(U_{jG}\right) < obj_{DE}\left(D_{i\_jG}\right) \\ D_{i\_jG}, & \text{otherwise} \end{cases} \tag{11}$$

VI. CASE STUDY

This section presents a case study for the application of the proposed AI-DT.

The specifications of the design conditions are listed in Table I. P_R is the rated output power and the adjustable range for P is

100W to 1000W. V_{2R} is the rated value of V_2 and the adjustable range for V_2 is 160V to 240V.

TABLE I. DESIGN CONDITIONS

Rated Conditions			
P_R	1000 W	V_1	200 V
V_{2R}	200 V	f_s	20 kHz
Adjustable Range			
P	100W-1000 W	V_2	160V-240 V
Switching Device			
Series	C2M0080120D, Cree	Dead Time	400 ns
$R_{DS(on)}$	80 $m\Omega$	V_{DSS}	1.2 kV
Isolated Transformer			
Inductor L_k		166.7 μH	

A. Phase One: Build Data-Driven Current Stress Models

With the flowchart in Fig. 9, XGBoost model can be built for current stress performance under different modulation strategies.

In Step 1, N_1, N_2, M_1 are set to be 20, 20 and 40. That means 20 samples, 20 samples and 40 samples are taken for P, V_2 and D_i, respectively. And thus the total number of combinations will be $3 \times N_1 \times N_2 \times M_1$ which is equal to 48000.

These combinations are run through PLECS simulation, and the corresponding current stress performance is recorded in Step 2. In Step 3, the one-class SVM is carefully adjusted to exclude most of outliers and keep normal data. The one-class SVM algorithm has two major hyperparameters: the kernel function and the soft margin coefficient υ. The kernel function indicates the nonlinear projection of input feature space to higher dimensional kernel space. Besides, as formularized in (4), the soft margin coefficient υ adjusts the effective radius. A larger coefficient υ means smaller radius of the decision boundary, excluding more outliers. The selected hyperparameters of one-class SVM given in Table II follow the recommendation in [49].

After the data trimming of Step 3, in the last step, a XGBoost model is trained with these clean simulation results. The clean simulation data after data trimming is partitioned into training set (60%), validation set (10%) and testing set (30%), which are used for training current stress model, selecting hyperparameters, and testing the trained XGBoost model on new and unseen data points, respectively. Among all the hyperparameters of XGBoost algorithms, learning rate, maximum tree depth, L2 regularization factor and number of estimators are adjusted since these hyperparameters have significant impacts on modeling accuracy. Possible model structures are enumerated to find the optimal one which achieves the lowest error on validation set. Some basic settings of XGBoost are listed in Table II.

TABLE II. SETTINGS OF ONE-CLASS SVM AND XGBOOST MODEL

Structure of One-Class SVM	
Kernel	Radial basis function
Soft margin coefficient υ	0.25
Structure of XGBoost Model	
Inputs	S, D_i, P, V_2
Output	Peak to peak current I_{pk}
Maximum depth of trees	8
Learning rate	0.1
L2 regularization factor	3
Number of estimators	1470

B. *Phase Two*: *Optimize Current Stress with DE Algorithm*

By following the flowchart in Fig. 12, DE algorithm will be adopted to find the optimal D_i and current stress performance for EPS1, EPS2 and DPS modulation strategies. Some key parameters in DE algorithm are listed in Table III.

The results of Phase Two are described graphically in the followings. Fig. 13, Fig. 14 and Fig. 15 give the optimal D_i value for EPS1, EPS2 and DPS modulation strategies.

TABLE III. SETTINGS OF DE ALGORITHM

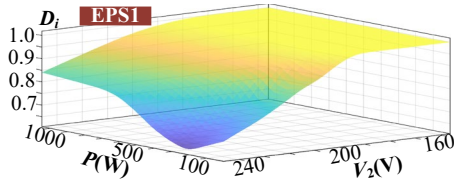| Structure of the Selected NN	
Inputs	S, D_i, P, V_2, XGBoost model $I_{pk}(S, D_i, P, V_2)$
Output	Minimal I_{pk} under given S, P, V_2
Population size NP	20
Maximum iterations	100
Differential weight F	0.5
Crossover rate CR	0.7

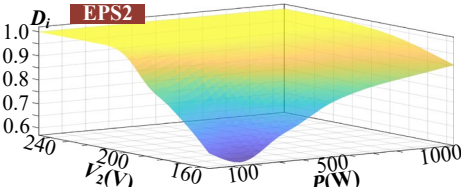Fig. 13. Optimal D_i for EPS1 given by the DE algorithm in Phase Two.

Fig. 14. Optimal D_i for EPS2 given by the DE algorithm in Phase Two.
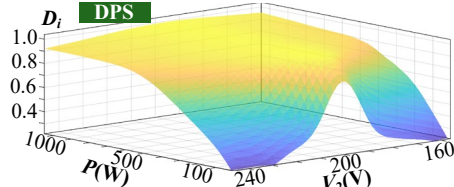

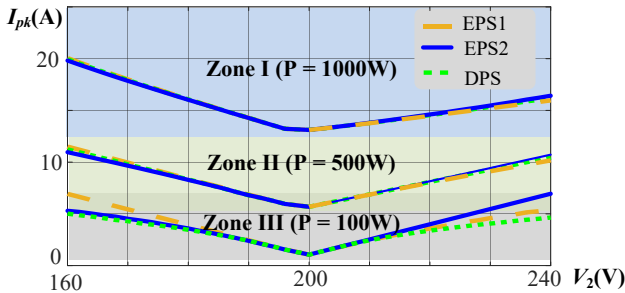Fig. 15. Optimal D_i for DPS given by the DE algorithm in Phase Two.

Fig. 16. Optimal current stress performance obtained by Phase Two.

The optimal current stress performance for these modulation strategies is shown in Fig. 16. Three power levels (100W, 500W, 1000W) have been taken for example as described as Zone I to Zone III. As we can find, at low power level ($P = 100$W), DPS gives best current stress performance in the full voltage range. While at medium and high power levels ($P = 500$W and 1000W), EPS2 stands out in buck mode ($V_2 < 200$V) and EPS1 outperforms the others in boost mode ($V_2 > 200$V). At the

boundary between buck and boost modes, three modulation strategies are optimized to be the same as SPS modulation, which has been validated in paper [50].
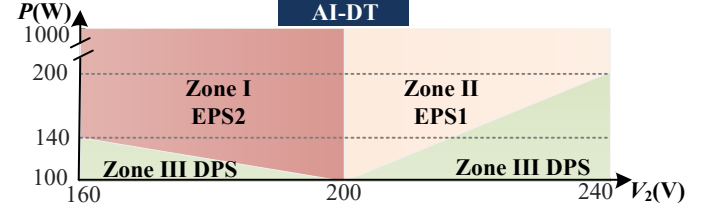

Fig. 17. The proposed AI-DT scheme in full voltage and power ranges.

Therefore, after comparing current stress performance of these three modulation strategies, the proposed AI-DT scheme in full voltage and power ranges can be obtained, as shown in Fig. 17. The optimal current stress of the proposed AI-DT is shown in Fig. 18. The control diagram to realize the proposed AI-DT is given in Fig. 19, where the outer phase shift D_o is regulated by the output of PI controller for closed-loop voltage and power regulation, the strategy selector selects the best strategy based on the results of Fig. 17, and the optimal modulation parameters of EPS1, EPS2, and DPS are provided in Fig. 13, Fig. 14, and Fig. 15, respectively.
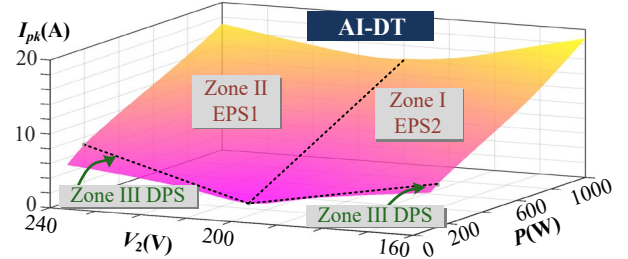

Fig. 18. Current stress performance of the proposed AI-DT scheme in full voltage and power ranges.
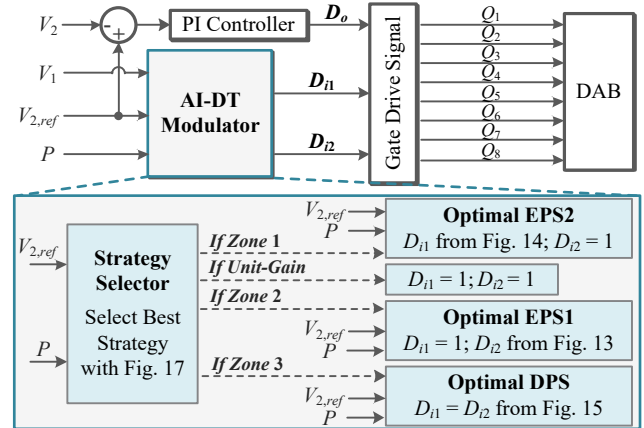

Fig. 19. Control diagram of the proposed AI-DT.

C. *Case Analysis*

As what shows in Fig. 13 to Fig. 17, when the voltage gain is closer to unit gain, the optimized modulation strategy tends towards SPS modulation. It proves that when the DAB converter operates with unit gain, SPS modulation enjoys the optimal performance in current stress, as discussed in [50].

Compared with DPS modulation, EPS modulation performs better at higher power level. The difference between DPS and

EPS is that DPS has three-level voltage in both v_{AB} and v_{CD} while EPS has two-level voltage in either v_{AB} or v_{CD}. The extra zero-voltage plateau in DPS helps relieve reverse current, but it also requires larger current to achieve a specific power level, leading to worse current stress performance at higher power level.

With regards to the selection of EPS1 and EPS2 in buck or boost mode, the three-level voltage should be applied to the higher voltage side. For example, in boost mode, EPS1 realizes a three-level voltage in the secondary side. This is because that the zero-voltage plateau in the higher voltage side helps eliminate more reactive power. As a result, it contributes to less circulating current and smaller current stress.

D. Computational Time and XGBoost Modeling Accuracy of the Design Case

The major advantage of the proposed AI-DT is its fully automation, where the model building process is automated with the one-class SVM and the specially adopted XGBoost, and the optimization process is automated with the DE algorithm. The proposed AI-DT can automate the conventional human-dependent design and accelerate the design cycle.

To reveal the computational time of AI-DT, the processing time of the computing platform of Intel Xeon E5-1630 with four CPU cores and 16 GB RAM is provided in Table IV. According to Table IV, 1 day and 3 hours are spent on running all 48000 simulations and the training of XGBoost models requires 6 minutes. The time of the automated modeling process of AI-DT is neglectable compared to the time-consuming manual derivation, which greatly reduces modulation design cycle.

TABLE IV. PROCESSING TIME OF AI-DT

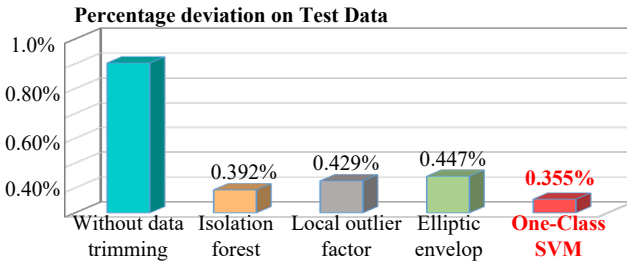| Phases	Computing Platform	Processing Time
Step 2 of Phase One: Run Simulations	Intel Xeon CPU E5-1630 with 16 GB RAM and 4 CPU cores	1 day and 3 hours
Step 3 of Phase One: XGBoost Training		6 minutes
Phase Two: Optimize Current Stress with DE		1 hour and 14 minutes

Fig. 20. Modeling accuracy with different data trimming techniques.

In addition, the negative impact of outliers and the better performance of the one-class SVM compared with other data trimming approaches are shown in Fig. 20. Without data trimming, the percentage deviation is 0.903%, while the deviation reduces significantly after applying data trimming, and the minimum deviation 0.355% is achieved with the adopted one-class SVM algorithm. As for the algorithm complexity, thanks to the inherent sparseness of support vector machine, the time and space complexity of one-class SVM is significantly better than others.
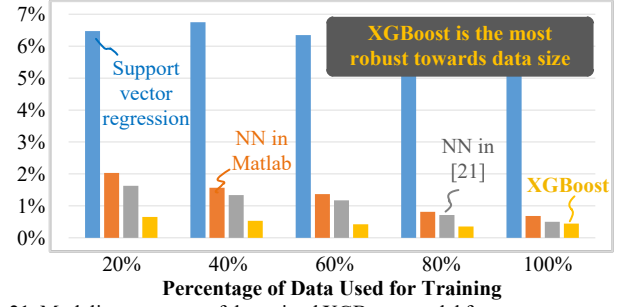

Fig. 21. Modeling accuracy of the trained XGBoost model for current stress with respect to different training data size.

Moreover, to validate the good performance of the specially adopted XGBoost model, the modeling accuracy of XGBoost with respect to different data size is evaluated and shown in Fig. 21. Three baselines are compared, including support vector regression, NN in Matlab toolbox, and NN in [27]. Among the regression models, the selected XGBoost model has the lowest percentage deviation on test data, which is only 0.355% given 100% of data for training. Moreover, when the percentage of training data decreases, the modeling accuracy of XGBoost is consistently good, lower than 0.7%. The comparisons in Fig. 21 justify the selection of XGBoost in the proposed AI-DT.
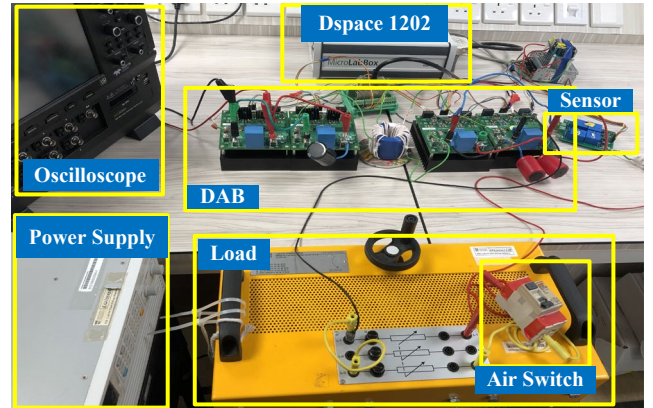
VII. EXPERIMENTAL VERIFICATION

Fig. 22. Prototype platform in the hardware experiments.

A hardware prototype has been designed to verify the effectiveness of the proposed AI-DT for the design case in Section VI, as shown in Fig. 22. The specifications of the experiments have been listed in Table I. Furthermore, the experimental set-up consists of a dSPACE RTI 1202 MicroLab box for modulation and control, a LeCroy WaveRunner providing voltage and current measurements, a power supply, and a variable resistive power load.

A. Operating Waveforms

The operating waveforms of different V_2 and P are listed below.

Fig. 23 gives the waveforms under rated operating conditions when P is 1000W and V_2 is 200V. Under this condition, the optimal modulation strategy is EPS1 with D_i equal to 1, which is same as SPS modulation. It can be seen that the DAB converter operates stably.
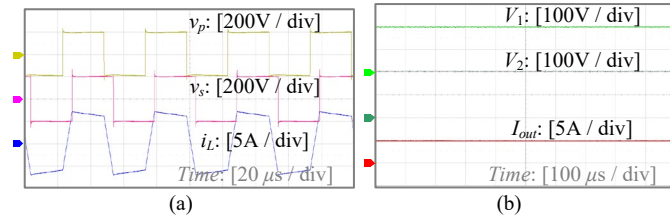
Fig. 23. Operating waveforms of the DAB convert under AI-DT when P is 1000W and V_2 is 200V: (a) v_p, i_L and v_s; (b) V_1, V_2 and I_{out}.

More operating conditions have been tested on this prototype. The modulation strategy and parameters for different conditions are decided with the proposed AI-DT method. Fig. 24 presents the operating waveforms of 500W and 100W when V_2 is 200V. The buck operating mode when V_2 is 160V is shown in Fig. 25, covering 1000W, 500W and 100W. And the boost operating mode when V_2 is 240V is shown in Fig. 26 for full power range.
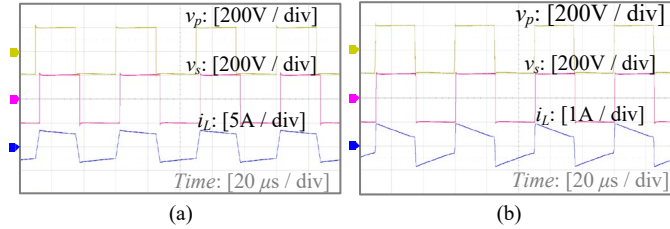

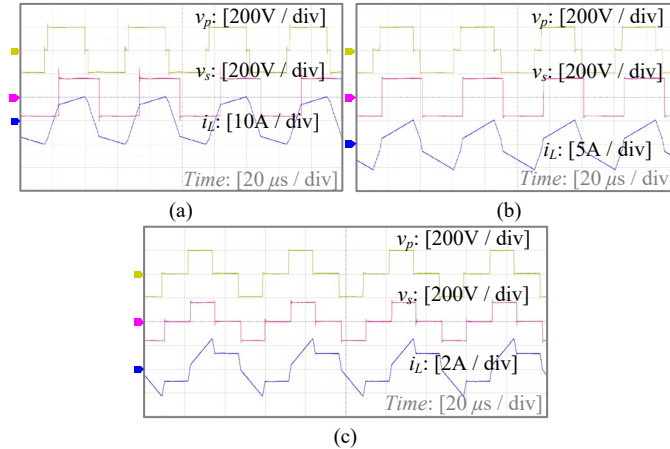Fig. 24. Operating waveforms of the DAB convert under AI-DT when V_2 is 200V: (a) $P = 500$W; (b) $P = 100$W.

Fig. 25. Operating waveforms of the DAB convert under AI-DT when V_2 is 160V: (a) $P = 1000$W; (b) $P = 500$W; (c) $P = 100$W.
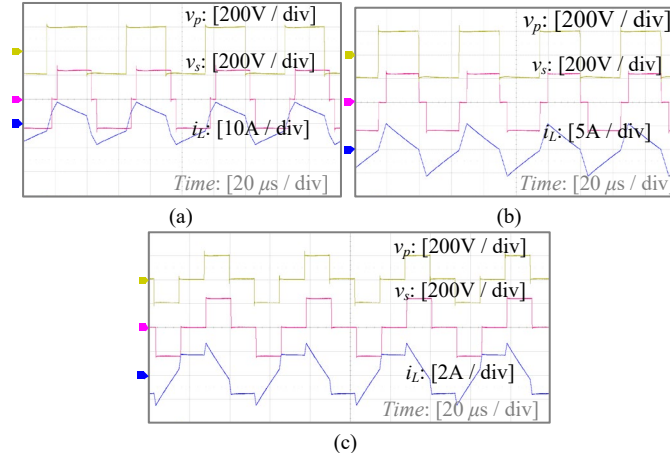

Fig. 26. Operating waveforms of the DAB convert under AI-DT when V_2 is

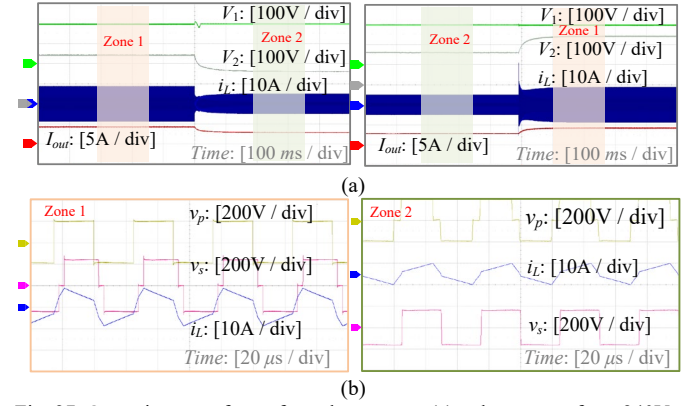240V: (a) $P = 1000$W; (b) $P = 500$W; (c) $P = 100$W.

B. Voltage and Load Step

Fig. 27. Operating waveforms for voltage steps: (a) voltage steps from 240V to 160V and then back to 240V; (b) zoom-in scope of v_p, v_s and i_L.

The experiments about voltage and load steps have also been conducted as shown below.

Fig. 28. Operating waveforms for load steps when V_2 is 240V: (a) output power steps from 500W to 1000W and then back to 500W; (b) zoom-in scope of v_p, v_s and i_L.

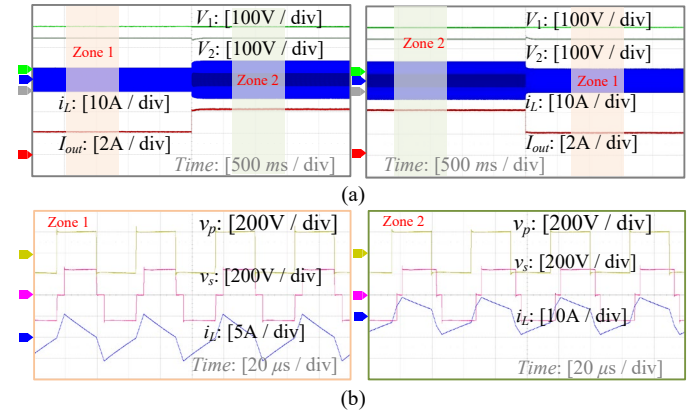Fig. 29. Operating waveforms for load steps when V_2 is 160V: (a) output power steps from 500W to 1000W and then back to 500W; (b) zoom-in scope of v_p, v_s and i_L.

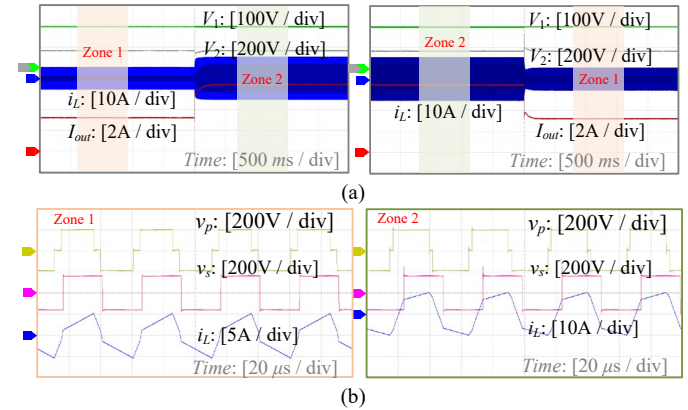In Fig. 27, when the DAB converter is operating at 240V and 1000W conditions, V_2 changes from 240V to 160V and back to 240V again. According to the proposed AI-DT, the modulation strategy will also switch. Fig. 27 (b) shows the zoom-in steady-

state waveforms of the two modulation strategies, thereby validating the hybrid operation under different operating conditions.

The waveforms of load step when V_2 is 240V and 160V are given in Fig. 28 and Fig. 29, respectively. The output power changes from 500W to 1000W and then back to 500W again. The zoom-in scopes for two operating zones are given in Fig. 28(b) and Fig. 29(b). It can be seen that the DAB converter exhibits speedy recovery after steps and the modulation methods are changed accordingly.

Therefore, the real-time operating capability of the proposed AI-DT approach is verified.

C. Current Stress, Zero Voltage Switching (ZVS) and Efficiency Performance of the Proposed AI-DT

Performance of the proposed AI-DT with regards to current stress, ZVS, and power efficiency is evaluated below.

Fig. 30 presents the results in the buck operating mode (V_2 = 160V). The performance of AI-DT integrates the best current stress performance of DPS and EPS together, so that the optimal current stress is always achieved in the full power range. The power efficiency has also been tested, which indicates good performance compared to single DPS, EPS or SPS modulation, too. The peak efficiency is above 96.5%. Fig. 31 gives the results in the boost operating mode (V_2 = 240V). The current stress performance of the proposed AI-DT is still optimal in the full power range, with the power efficiency matching or exceeding the ones for the individual modulation strategies. The peak power efficiency is measured to be above 96.0%. Additionally, the current stress performance and power efficiency performance of AI-DT under unit gain (V_2 = 200V) are plotted in Fig. 32.
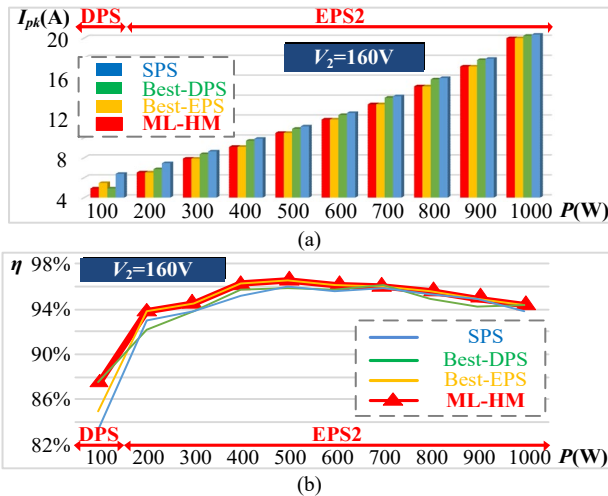

Fig. 30. Experimental current stress (I_{pk}) and efficiency (η) of SPS, best DPS, best EPS, and the proposed AI-DT when V_2 is 160V: (a) I_{pk}; (b) η.

The optimization of current stress performance can broaden the ZVS range in the meantime. As the waveforms of v_p, v_s, and i_L shown in Fig. 23 and Fig. 24, under unit-gain mode, ZVS of all 8 switches has been satisfied. Under buck mode shown in Fig. 25, all-switch ZVS is realized for medium and high power, and the optimal DPS adopted in 100 W achieves ZVS for 6 switches (Q_1~ Q_4, Q_7, Q_8), while ZVS for Q_5 and Q_6 is not satisfied.

Under light load conditions, DPS slightly sacrifices the ZVS performance to reach optimal current stress. For boost operation shown in Fig. 26, the optimal EPS1 realizes full ZVS for 1000 W and 500 W, and 6 switches attain ZVS under light load conditions.
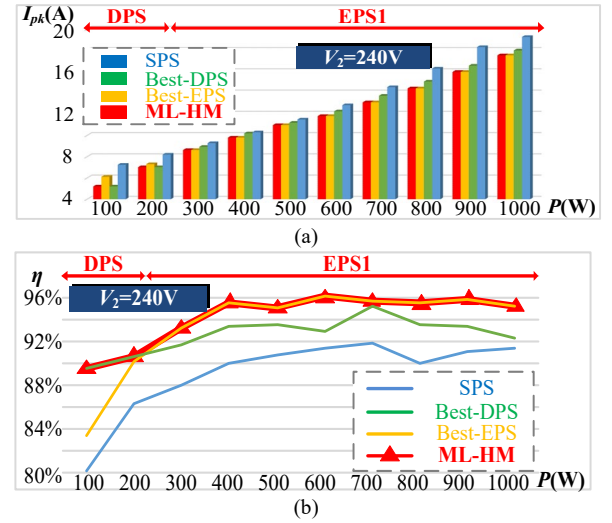

Fig. 31. Experimental current stress (I_{pk}) and efficiency (η) of SPS, best DPS, best EPS, and the proposed AI-DT when V_2 is 240V: (a) I_{pk}; (b) η.
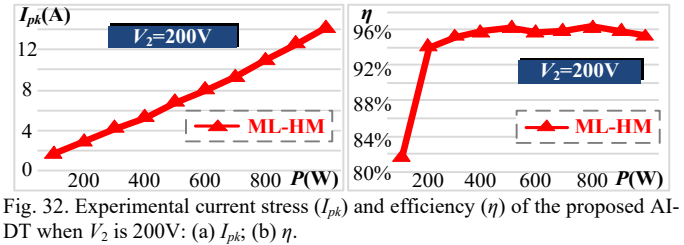
Fig. 32. Experimental current stress (I_{pk}) and efficiency (η) of the proposed AI-DT when V_2 is 200V: (a) I_{pk}; (b) η.

As shown in these figures, the superiority of the proposed AI-DT is obvious when the DAB converter is not operating at unit gain. The proposed AI-DT is able to realize optimal current stress performance in the full voltage and full power ranges with only two degrees of freedom in modulation implementation.

To prove the satisfactory modeling accuracy of the proposed AI-DT approach, the theoretical current stress performance evaluated by the trained XGBoost models is compared with experimental results. As shown in Fig. 33, the theoretical current stress I_{pk} given by XGBoost models only has 2.2% accuracy difference from experimental results on average, which is mainly caused by environmental noise. Hence, the modeling of AI-DT approach is in accordance with experiments, and the potential model discrepancy is handled in this article.

Fig. 33. Comparison between theoretical current stress performance evaluated by XGBoost models and experimental performance.

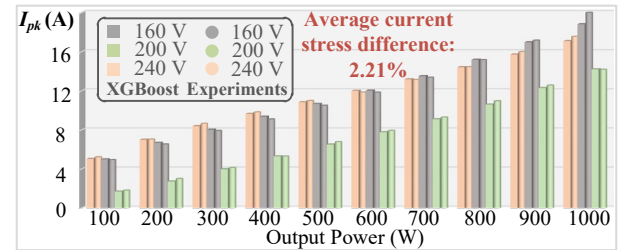To sum up, the experimental results above have empirically validated the feasibility and excellence of the proposed AI-DT comprehensively.

VIII. CONCLUSION

In this paper, an AI-based design with data trimming (AI-DT) for hybrid phase shift modulation is proposed, which combines two two-degree-of freedom modulation strategies, EPS and DPS. This proposed AI-DT approach is able to optimize current stress performance of the DAB converter. Besides that, the proposed AI-DT is developed automatically with the assistance of AI tools, which alleviate the negative influence of outliers, improve modeling accuracy, and relieve heavy computation loads. Generally, the proposed AI-DT approach consists of two phases. In the first phase, the one-class SVM algorithm is adopted to exclude outliers for data trimming, and the extreme gradient boosting technique is used to develop a data-driven current stress model for the DAB converter. In the second phase, differential evolution algorithm is adopted to find optimal modulation strategy parameter for a specific operating condition. The effectiveness of the proposed AI-DT approach has been validated by 1kW hardware experiments, in which the optimal current stress is realized under full operating conditions.

The crucial key to attain high modeling accuracy is to ensure that the built simulation model accords well with the experimental results. To mitigate threats posed by model discrepancy, the following directions can be investigated in the future. First, instead of using simulation data, experiments can be practical data source for data-driven modeling. Furthermore, the hybrid combination of simulation data and experiments can be explored. Moreover, modern AI structures like attention neural networks, physics-informed neural networks, multi-task learning can be retrofitted to facilitate the practicality of data-driven models.

REFERENCES

[1] R. W. A. A. De Doncker, D. M. Divan, and M. H. Kheraluwala, 'A three-phase soft-switched high-power-density DC/DC converter for high-power applications', *IEEE Trans. Ind. Appl.*, vol. 27, no. 1, pp. 63–73, Feb. 1991, doi: 10.1109/28.67533.

[2] M. N. Kheraluwala, R. W. Gascoigne, D. M. Divan, and E. D. Baumann, 'Performance characterization of a high-power dual active bridge DC-to-DC converter', *IEEE Trans. Ind. Appl.*, vol. 28, no. 6, pp. 1294–1301, Dec. 1992, doi: 10.1109/28.175280.

[3] Y. Hu *et al.*, 'High-Frequency-Link Current Stress Optimization of Cascaded H-Bridge-Based Solid-State Transformer With Third-Order Harmonic Voltage Injection', *IEEE J. Emerg. Sel. Top. Power Electron.*, vol. 9, no. 1, pp. 1027–1038, Feb. 2021, doi: 10.1109/JESTPE.2020.2965232.

[4] I. Alhurayyis, A. Elkhateb, and J. Morrow, 'Isolated and Nonisolated DC-to-DC Converters for Medium-Voltage DC Networks: A Review', *IEEE J. Emerg. Sel. Top. Power Electron.*, vol. 9, no. 6, pp. 7486–7500, Dec. 2021, doi: 10.1109/JESTPE.2020.3028057.

[5] M. Shousha, A. Prodic, V. Marten, and J. Milios, 'Design and Implementation of Assisting Converter-Based Integrated Battery Management System for Electromobility Applications', *IEEE J. Emerg. Sel. Top. Power Electron.*, vol. 6, no. 2, pp. 825–842, Jun. 2018, doi: 10.1109/JESTPE.2017.2736166.

[6] H. Akagi and R. Kitada, 'Control and Design of a Modular Multilevel Cascade BTB System Using Bidirectional Isolated DC/DC Converters',

[7] F. Lin, X. Zhang, and X. Li, 'Design Methodology for Symmetric CLLC Resonant DC Transformer Considering Voltage Conversion Ratio, System Stability, and Efficiency', *IEEE Trans. Power Electron.*, vol. 36, no. 9, pp. 10157–10170, Sep. 2021, doi: 10.1109/TPEL.2021.3059852.

[8] D. Dong, M. Agamy, J. Z. Bebic, Q. Chen, and G. Mandrusiak, 'A Modular SiC High-Frequency Solid-State Transformer for Medium-Voltage Applications: Design, Implementation, and Testing', *IEEE J. Emerg. Sel. Top. Power Electron.*, vol. 7, no. 2, pp. 768–778, Jun. 2019, doi: 10.1109/JESTPE.2019.2896046.

[9] A. Tuluhong, W. Wang, Y. Li, H. Wang, and L. Xu, 'Parasitic Parameter Extraction and Identification Method for HFT based on DC-DC Converter in EV Application', *IEEE J. Emerg. Sel. Top. Power Electron.*, pp. 1–1, 2021, doi: 10.1109/JESTPE.2021.3136777.

[10] F. Krismer and J. W. Kolar, 'Accurate Small-Signal Model for the Digital Control of an Automotive Bidirectional Dual Active Bridge', *IEEE Trans. Power Electron.*, vol. 24, no. 12, pp. 2756–2768, Dec. 2009, doi: 10.1109/TPEL.2009.2027904.

[11] B. Zhao, Q. Song, and W. Liu, 'Power Characterization of Isolated Bidirectional Dual-Active-Bridge DC–DC Converter With Dual-Phase-Shift Control', *IEEE Trans. Power Electron.*, vol. 27, no. 9, pp. 4172–4176, Sep. 2012, doi: 10.1109/TPEL.2012.2189586.

[12] B. Zhao, Q. Yu, and W. Sun, 'Extended-Phase-Shift Control of Isolated Bidirectional DC–DC Converter for Power Distribution in Microgrid', *IEEE Trans. Power Electron.*, vol. 27, no. 11, pp. 4667–4680, Nov. 2012, doi: 10.1109/TPEL.2011.2180928.

[13] J. Tian, F. Wang, F. Zhuo, Y. Wang, H. Wang, and Y. Li, 'A Zero-Backflow-Power EPS Control Scheme with Multi-Objective Coupled-Relationship Optimization in DAB Based Converter', *IEEE J. Emerg. Sel. Top. Power Electron.*, pp. 1–1, 2021, doi: 10.1109/JESTPE.2021.3126435.

[14] S. S. Muthuraj, V. K. Kanakesh, P. Das, and S. K. Panda, 'Triple Phase Shift Control of an LLL Tank Based Bidirectional Dual Active Bridge Converter', *IEEE Trans. Power Electron.*, vol. 32, no. 10, pp. 8035–8053, Oct. 2017, doi: 10.1109/TPEL.2016.2637506.

[15] Y. Shen, X. Sun, W. Li, X. Wu, and B. Wang, 'A Modified Dual Active Bridge Converter With Hybrid Phase-Shift Control for Wide Input Voltage Range', *IEEE Trans. Power Electron.*, pp. 1–1, 2015, doi: 10.1109/TPEL.2015.2510033.

[16] A. K. Bhattacharjee and I. Batarseh, 'Optimum Hybrid Modulation for Improvement of Efficiency Over Wide Operating Range for Triple-Phase-Shift Dual-Active-Bridge Converter', *IEEE Trans. Power Electron.*, vol. 35, no. 5, pp. 4804–4818, May 2020, doi: 10.1109/TPEL.2019.2943392.

[17] D. Mou *et al.*, 'Hybrid Duty Modulation for Dual Active Bridge Converter to Minimize RMS Current and Extend Soft-Switching Range Using the Frequency Domain Analysis', *IEEE Trans. Power Electron.*, vol. 36, no. 4, pp. 4738–4751, Apr. 2021, doi: 10.1109/TPEL.2020.3022416.

[18] F. Lin, X. Zhang, X. Li, L. Chaohui, and H. Ma, 'Parameter Design for Symmetrical CLLC-Type DC Transformer Considering Cascaded System Stability and Power Efficiency', *IEEE J. Emerg. Sel. Top. Power Electron.*, vol. 9, no. 5, pp. 6219–6231, Oct. 2021, doi: 10.1109/JESTPE.2020.3034402.

[19] X. Shen, T. Ouyang, Z. Chen, S. Zhao, J. Fang, and Y. Zhang, 'Randomized Computation for the Current Stress Policy Design in the DAB Converter', *IEEE Control Syst. Lett.*, vol. 5, no. 3, pp. 863–868, Jul. 2021, doi: 10.1109/LCSYS.2020.3006398.

[20] Y. Tang *et al.*, 'Artificial Intelligence-Aided Minimum Reactive Power Control for the DAB Converter Based on Harmonic Analysis Method', *IEEE Trans. Power Electron.*, vol. 36, no. 9, pp. 9704–9710, Sep. 2021, doi: 10.1109/TPEL.2021.3059750.

[21] Y. Tang *et al.*, 'RL-ANN-Based Minimum-Current-Stress Scheme for the Dual-Active-Bridge Converter With Triple-Phase-Shift Control', *IEEE J. Emerg. Sel. Top. Power Electron.*, vol. 10, no. 1, pp. 673–689, Feb. 2022, doi: 10.1109/JESTPE.2021.3071724.

[22] Q. Sun, Y. Wang, and Y. Jiang, 'A Novel Fault Diagnostic Approach for DC-DC Converters Based on CSA-DBN', *IEEE Access*, vol. 6, pp. 6273–6285, 2018, doi: 10.1109/ACCESS.2017.2786458.

[23] M. Hajihosseini, M. Andalibi, M. Gheisarnejad, H. Farsizadeh, and M.-H. Khooban, 'DC/DC Power Converter Control-Based Deep Machine Learning Techniques: Real-Time Implementation', *IEEE Trans. Power*

IEEE JOURNAL OF EMERGING AND SELECTED TOPICS IN POWER ELECTRONICS

Electron., vol. 35, no. 10, pp. 9971–9977, Oct. 2020, doi: 10.1109/TPEL.2020.2977765.

[24] H. Zhang, X. Tong, and J. Yin, 'Optimal triple-phase-shift controller design of isolated bidirectional DC-DC converter based on ant colony algorithm and BP neural network', in *IECON 2017 - 43rd Annual Conference of the IEEE Industrial Electronics Society*, Beijing, Oct. 2017, pp. 8802–8807. doi: 10.1109/IECON.2017.8217547.

[25] X. Li, X. Zhang, F. Lin, and F. Blaabjerg, 'Artificial-Intelligence-Based Design (AI-D) for Circuit Parameters of Power Converters', *IEEE Trans. Ind. Electron.*, pp. 1–1, 2021, doi: 10.1109/TIE.2021.3088377.

[26] X. Li, X. Zhang, F. Lin, C. Sun, and K. Mao, 'Artificial-Intelligence-Based Triple Phase Shift Modulation for Dual Active Bridge Converter with Minimized Current Stress', *IEEE J. Emerg. Sel. Top. Power Electron.*, pp. 1–1, 2021, doi: 10.1109/JESTPE.2021.3105522.

[27] F. Lin, X. Zhang, X. Li, C. Sun, W. Cai, and Z. Zhang, 'Automatic Triple Phase-Shift Modulation for DAB Converter With Minimized Power Loss', *IEEE Trans. Ind. Appl.*, vol. 58, no. 3, pp. 3840–3851, May 2022, doi: 10.1109/TIA.2021.3136501.

[28] M. Gupta, J. Gao, C. C. Aggarwal, and J. Han, 'Outlier Detection for Temporal Data: A Survey', *IEEE Trans. Knowl. Data Eng.*, vol. 26, no. 9, pp. 2250–2267, Sep. 2014, doi: 10.1109/TKDE.2013.184.

[29] H. Guo, S. Li, B. Li, Y. Ma, and X. Ren, 'A New Learning Automata-Based Pruning Method to Train Deep Neural Networks', *IEEE Internet Things J.*, vol. 5, no. 5, pp. 3263–3269, Oct. 2018, doi: 10.1109/JIOT.2017.2711426.

[30] X. Xu, Y. Lei, and Z. Li, 'An Incorrect Data Detection Method for Big Data Cleaning of Machinery Condition Monitoring', *IEEE Trans. Ind. Electron.*, vol. 67, no. 3, pp. 2326–2336, Mar. 2020, doi: 10.1109/TIE.2019.2903774.

[31] C. Lee, S. Jo, D. Kwon, and M. G. Pecht, 'Capacity-Fading Behavior Analysis for Early Detection of Unhealthy Li-Ion Batteries', *IEEE Trans. Ind. Electron.*, vol. 68, no. 3, pp. 2659–2666, Mar. 2021, doi: 10.1109/TIE.2020.2972468.

[32] J. Ma, Z. Teng, Q. Tang, W. Qiu, Y. Yang, and J. Duan, 'Measurement Error Prediction of Power Metering Equipment Using Improved Local Outlier Factor and Kernel Support Vector Regression', *IEEE Trans. Ind. Electron.*, vol. 69, no. 9, pp. 9575–9585, Sep. 2022, doi: 10.1109/TIE.2021.3114740.

[33] T. Chen and C. Guestrin, 'XGBoost: A Scalable Tree Boosting System', in *Proceedings of the 22nd ACM SIGKDD International Conference on Knowledge Discovery and Data Mining*, San Francisco California USA, Aug. 2016, pp. 785–794. doi: 10.1145/2939672.2939785.

[34] B. Zhao, Q. Song, W. Liu, and Y. Sun, 'Overview of Dual-Active-Bridge Isolated Bidirectional DC–DC Converter for High-Frequency-Link Power-Conversion System', *IEEE Trans. Power Electron.*, vol. 29, no. 8, pp. 4091–4106, Aug. 2014, doi: 10.1109/TPEL.2013.2289913.

[35] G. Chen, Z. Chen, Y. Chen, C. Feng, and X. Zhu, 'Comprehensive analysis of asymmetric modulated Dual-Active-Bridge converter and its Hybrid control strategy', *IEEE J. Emerg. Sel. Top. Power Electron.*, pp. 1–1, 2021, doi: 10.1109/JESTPE.2021.3135288.

[36] O. Kwon, K.-S. Kim, and B.-H. Kwon, 'Highly Efficient Single-Stage DAB Microinverter Using a Novel Modulation Strategy to Minimize Reactive Power', *IEEE J. Emerg. Sel. Top. Power Electron.*, vol. 10, no. 1, pp. 544–552, Feb. 2022, doi: 10.1109/JESTPE.2021.3090097.

[37] G. G. Oggier, G. O. GarcÍa, and A. R. Oliva, 'Switching Control Strategy to Minimize Dual Active Bridge Converter Losses', *IEEE Trans. Power Electron.*, vol. 24, no. 7, pp. 1826–1838, Jul. 2009, doi: 10.1109/TPEL.2009.2020902.

[38] B. Zhao, Q. Song, W. Liu, and W. Sun, 'Current-Stress-Optimized Switching Strategy of Isolated Bidirectional DC–DC Converter With Dual-Phase-Shift Control', *IEEE Trans. Ind. Electron.*, vol. 60, no. 10, pp. 4458–4467, Oct. 2013, doi: 10.1109/TIE.2012.2210374.

[39] B. Zhao, Q. Song, and W. Liu, 'Efficiency Characterization and Optimization of Isolated Bidirectional DC–DC Converter Based on Dual-Phase-Shift Control for DC Distribution Application', *IEEE Trans. Power Electron.*, vol. 28, no. 4, pp. 1711–1727, Apr. 2013, doi: 10.1109/TPEL.2012.2210563.

[40] B. Zhao, Q. Song, W. Liu, G. Liu, and Y. Zhao, 'Universal High-Frequency-Link Characterization and Practical Fundamental-Optimal Strategy for Dual-Active-Bridge DC-DC Converter Under PWM Plus Phase-Shift Control', *IEEE Trans. Power Electron.*, vol. 30, no. 12, pp. 6488–6494, Dec. 2015, doi: 10.1109/TPEL.2015.2430934.

[41] A. K. Jain and R. Ayyanar, 'Pwm control of dual active bridge: Comprehensive analysis and experimental verification', *IEEE Trans. Power Electron.*, vol. 26, no. 4, pp. 1215–1227, Apr. 2011, doi: 10.1109/TPEL.2010.2070519.

[42] A. Tong, L. Hang, G. Li, X. Jiang, and S. Gao, 'Modeling and Analysis of a Dual-Active-Bridge-Isolated Bidirectional DC/DC Converter to Minimize RMS Current With Whole Operating Range', *IEEE Trans. Power Electron.*, vol. 33, no. 6, pp. 5302–5316, Jun. 2018, doi: 10.1109/TPEL.2017.2692276.

[43] A. Garcia-Bediaga, I. Villar, A. Rujas, I. Etxeberria-Otadui, and A. Rufer, 'Analytical Models of Multiphase Isolated Medium-Frequency DC–DC Converters', *IEEE Trans. Power Electron.*, vol. 32, no. 4, pp. 2508–2520, Apr. 2017, doi: 10.1109/TPEL.2016.2570941.

[44] M. N. H. Khan, M. Forouzesh, Y. P. Siwakoti, L. Li, T. Kerekes, and F. Blaabjerg, 'Transformerless Inverter Topologies for Single-Phase Photovoltaic Systems: A Comparative Review', *IEEE J. Emerg. Sel. Top. Power Electron.*, vol. 8, no. 1, pp. 805–835, Mar. 2020, doi: 10.1109/JESTPE.2019.2908672.

[45] S. Das and P. N. Suganthan, 'Differential Evolution: A Survey of the State-of-the-Art', *IEEE Trans. Evol. Comput.*, vol. 15, no. 1, pp. 4–31, Feb. 2011, doi: 10.1109/TEVC.2010.2059031.

[46] V. Kachitvichyanukul, 'Comparison of Three Evolutionary Algorithms: GA, PSO, and DE', *Ind. Eng. Manag. Syst.*, vol. 11, no. 3, pp. 215–223, Sep. 2012, doi: 10.7232/iems.2012.11.3.215.

[47] D. Fodorean, L. Idoumghar, M. Brevilliers, P. Minciunescu, and C. Irimia, 'Hybrid Differential Evolution Algorithm Employed for the Optimum Design of a High-Speed PMSM Used for EV Propulsion', *IEEE Trans. Ind. Electron.*, vol. 64, no. 12, pp. 9824–9833, Dec. 2017, doi: 10.1109/TIE.2017.2701788.

[48] Y. Mao and S. Niu, 'Topology Exploration and Analysis of a Novel Winding Factor Modulation Based Hybrid-Excited Biased-Flux Machine', *IEEE J. Emerg. Sel. Top. Power Electron.*, pp. 1–1, 2021, doi: 10.1109/JESTPE.2021.3071923.

[49] S. S. Khan and M. G. Madden, 'One-class classification: taxonomy of study and review of techniques', *Knowl. Eng. Rev.*, vol. 29, no. 3, pp. 345–374, Jun. 2014, doi: 10.1017/S026988891300043X.

[50] O. M. Hebala, A. A. Aboushady, K. H. Ahmed, and I. Abdelsalam, 'Generic Closed-Loop Controller for Power Regulation in Dual Active Bridge DC–DC Converter With Current Stress Minimization', *IEEE Trans. Ind. Electron.*, vol. 66, no. 6, pp. 4468–4478, Jun. 2019, doi: 10.1109/TIE.2018.2860535.